ACS NANO

www.acsnano.org

ARTICLE

4D Printing of Silica Glass Microstructures Based on Capillary-Force-Assisted Assembly

Yuan Tao,[⊥] Rui Li,[⊥] Zhaoxin Lao, Yusheng Jin, Hao Wu, Zeheng Wu, Wei Zeng, Modong Jiang, Jincheng Ni, Yanlei Hu,* Dong Wu, Jiaru Chu, and Jiawen Li*

Cite This: *ACS Nano* 2025, 19, 40547−40560

Read Online

ACCESS | Metrics & More | Article Recommendations | Supporting Information

ABSTRACT: **Four-dimensional (4D) printing enables simple structures to undergo programmed and controlled morphological reconfiguration for fabricating more complex three-dimensional (3D) architectures, which has recently garnered considerable research interest. However, 4D printing of glass, particularly for glass microstructures, faces fundamental challenges due to the limited deformability of glass and the lack of reliable deformation mechanisms. Here, a capillary-force-assisted assembly approach is presented to realize the 4D printing of glass microstructures with programmable morphing capabilities. The precursor microstructures fabricated by two-photon polymerization are reconfigured into complex 3D microassemblies under postprinting capillary force, ultimately yielding transparent glass microstructures upon thermal sintering. Compared with conventional 3D printing approaches, our 4D printing approach enables the fabrication of geometrically sophisticated glass microstructures, particularly development-resistant geometries such as hollow microarchitectures, which are previously unattainable through additive manufacturing techniques. Furthermore, the fabricated glass-based chiroptical metamaterials demonstrate giant chiroptical responses and enhanced environmental stability when compared to conventional polymeric counterparts. Fully enclosed hollow microarchitectures successfully encapsulate a diversity of inorganic particles. This work provides a scalable platform for advanced glass microfabrication and allows for the 4D printing of functional inorganic devices.**

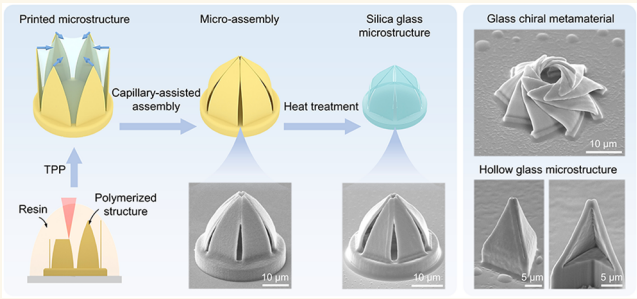

KEYWORDS: *4D printing, capillary-force-assisted assembly, glass microstructures, two-photon polymerization, chiroptical metamaterials, hollow microstructures*

Four-dimensional (4D) printing is a transformative additive manufacturing technology that leverages structural configurations with deformable properties, enabling programmed and controlled morphological reconfiguration of printed architectures[1,2] through temperature,[3−5] humidity,[6−8] light,[9−11] cell contractile force,[12] or mechanical force.[13,14] The technology provides a simple and efficient approach to construct complex three-dimensional (3D) architectures from simple geometries by leveraging programmable material behavior.[15] Compared to conventional 3D printing, 4D printing offers access to more delicate and hierarchical structures, such as curved thin-walled,[14] large-span,[16] and hollow structures,[17] which present fabrication challenges for conventional direct 3D printing techniques. A wide range of materials have been successfully adapted for 4D printing, including organic materials such as hydrogel,[12,18,19] shape memory polymer,[20] and hard and brittle inorganic materials like ceramics.[21−35] Therefore, 4D printing offers unprecedented opportunities for the fabrication of 3D structures with diverse functional materials.

Silica glass, renowned for its exceptional optical transparency, mechanical robustness, thermal stability, and chemical inertness, remains indispensable in advanced industrial and scientific applications.[36−38] 3D complex glass structures with micro/nano features can be achieved by integrating organic−inorganic silica precursor 3D printing with subsequent thermal treatment,[39−41] which have demonstrated significant potential in micro-optics,[42,43] photonics,[44,45] micromechanics,[46] and microfluidics.[47] However, 4D printing of glass remains underexplored. To address this research gap, insights can be drawn from well-established ceramic 4D printing strategies, which primarily rely on anisotropic shrinkage[21−26] or external

Received: September 6, 2025
Revised: November 11, 2025
Accepted: November 12, 2025
Published: November 18, 2025

https://doi.org/10.1021/acsnano.5c15343
ACS Nano 2025, 19, 40547−40560

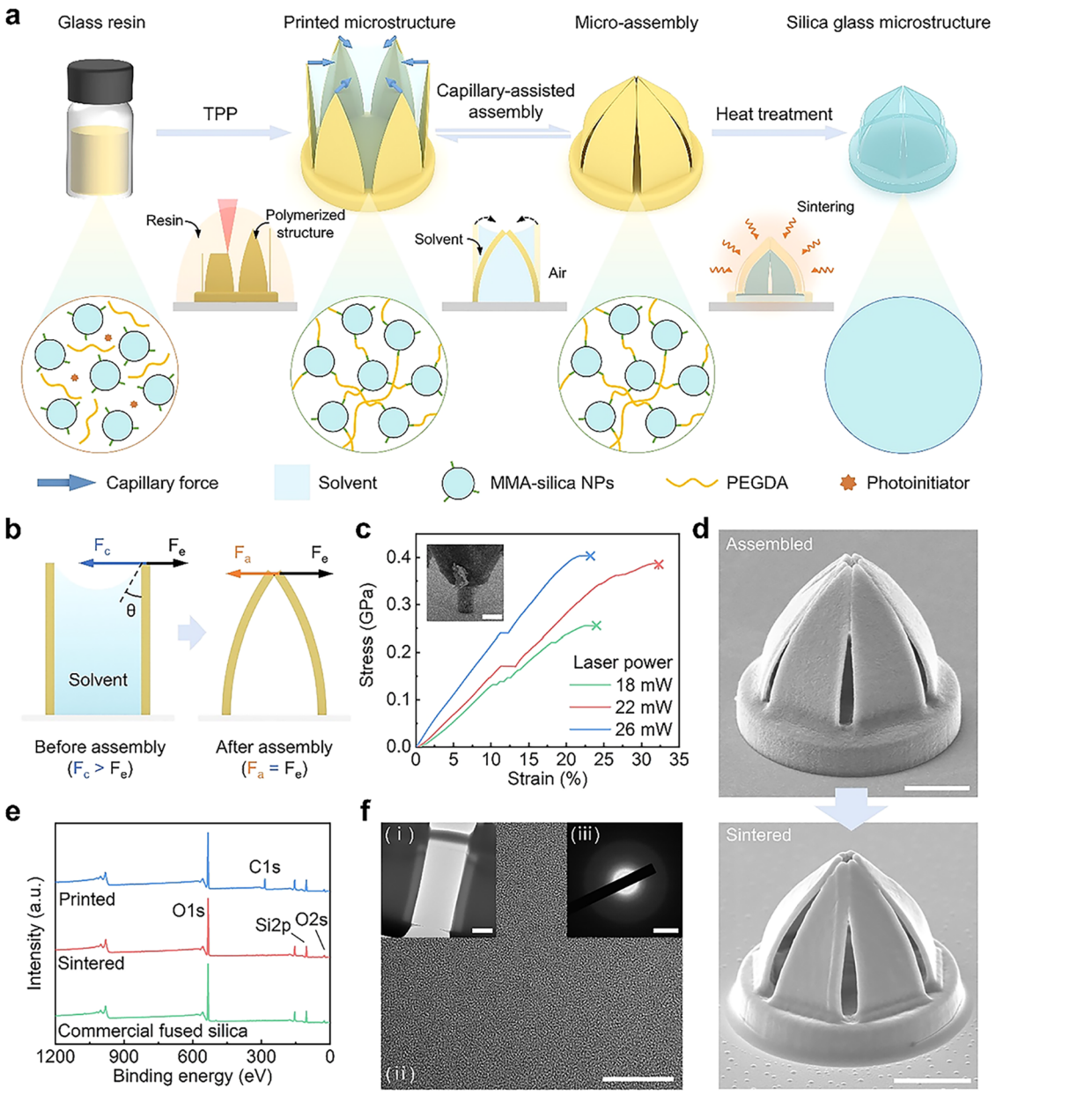

Figure 1. General process for 4D printing of silica glass microstructures. (a) Schematic illustration of fabricating glass microassembly through TPP, capillary-force-assisted assembly, and heat treatment. (b) Schematic illustration of force analysis during capillary-force-assisted assembly of printed microplates. (c) Stress−strain curves of printed micropillars with different laser processing power. Scale bar: 5 μm. (d) SEM images of the assembled and sintered six-petal thin-walled microstructure. Scale bars: 10 μm. (e) XPS of the printed samples, sintered glass, and commercial fused silica glass. (f) Bright-field TEM images and a selected area diffraction pattern of the sintered glass. Scale bars: (i) 1 μm, (ii) 20 nm, and (iii) 5 nm^{-1}.

mechanical actuation.[27−35] These approaches induce controlled deformation of 3D-printed structures either after printing or during thermal treatment, which typically necessitate silica precursors with sufficient deformability. Although increasing the organic content improves precursor deformability, this compositional modification significantly reduces solid loading, leading to sintering-induced excessive shrinkage and geometric distortion. Moreover, these deformation mechanisms cannot be readily extended to the micro/nanoscale due to the incompatible force-structure relationship and inherent operational challenges at microscopic dimensions. In anisotropic-shrinkage-driven methods, the mismatch between driving forces and structural rigidity exists, while external mechanical actuation fails to achieve the precision required for microscale manipulation. Additionally, the transition to microscale dimensions amplifies the impact of minor fabrication errors, thereby severely compromising deformation accuracy. Achieving high-quality 4D printing of glass structures at these finer scales remains a critical challenge, as it demands a fundamentally different driving force capable of precise deformation without compromising microstructural integrity.

At the microscale, current 4D printing is confined to stimulus-responsive organic materials.[11,18,48,49] The incorporation of inorganic components can severely compromise their deformability, which makes them unsuitable for 4D printing of

https://doi.org/10.1021/acsnano.5c15343
ACS Nano 2025, 19, 40547−40560

inorganic materials. To drive structural deformation at the micro/nanoscale, capillary-force-induced self-assembly techniques have attracted significant research interest.[50,51] Capillary force arises from liquid meniscus formation at the solid−liquid interface during liquid evaporation and spontaneously emerges without requiring external energy input. This force is on the order of millinewtons, which is apt for inducing deformation in microstructures.[52−55] Under capillary action, complex 3D microarchitectures can be precisely assembled from microunits (e.g., micropillars, microplates), with their assembly morphology being flexibly adjustable by altering the dimensions, geometries, and spatial arrangements of the microunits.[56−58] For instance, 3D hierarchical structures[59−61] and microchannels[62] can be assembled by laser-printed micropillars and microplates. Besides, chiral microstructures can be formed through asymmetrical capillary force induced by micropillars with asymmetric cross sections or initial bending angles.[57,63−67] These assembled microstructures hold significant application prospects in particle trapping,[59−61] chiral sensing,[63−67] cell cluster culture,[68] and microfluidics.[62,69] Therefore, capillary force is anticipated to be an ideal mechanism for driving silica precursor deformation and enabling the 4D printing of glass microstructures. However, existing capillary-force-driven assembly has been predominantly limited to organic or low-inorganic-content materials, leaving a significant gap in achieving high-inorganic-content structures essential for functional glass devices.

Here, we present a 4D printing approach for fabricating high-quality glass microstructures through capillary-force-assisted assembly of two-photon polymerization (TPP)-printed organic−inorganic hybrid silica precursors, followed by thermal conversion to fused silica glass. Our approach establishes a comprehensive "material-force-structure" relationship for TPP-based 4D printing of inorganic−organic hybrid material, specifically addressing the challenge of matching capillary forces with the mechanical properties of high-inorganic-content precursors. Through systematic optimization of material composition and printing parameters, we achieve precise control over precursor deformability while maintaining sufficient inorganic content to minimize sintering distortion. Furthermore, we identify and characterize a sintering-induced "welding" effect that transitions interfacial bonding from weak physical adhesion to robust covalent fusion, ensuring permanent structural stability. Based on this approach, we fabricate diverse glass microassemblies with submicron feature resolution, including hierarchical microstructures, chiral metamaterials, long microchannels, and hollow microarchitectures. The 4D-printed chiroptical metamaterials exhibit giant chiroptical responses and enhanced environmental stability. Particularly noteworthy are the fully enclosed hollow microstructures, which overcome the inherent limitation of conventional 3D printing, namely, the inability to develop inaccessible internal regions, and are successfully utilized to encapsulate inorganic particles (yttrium, lanthanum, and zirconium oxides). We also fabricate semienclosed microchannels that show potential applications in microfluidics. These results collectively demonstrate that the proposed approach successfully applies the 4D printing concept to the fabrication of high-performance inorganic microstructures, suggesting its potential for advancing glass microfabrication.

RESULTS AND DISCUSSION

4D Printing of Silica Glass Microstructures. Figure 1a illustrates the process for 4D printing of glass microstructures based on capillary-force-assisted assembly. First, a glass precursor composed of silica nanoparticles (NPs) and polymer matrix is printed using TPP according to the designed shape, as exemplified by the six-petal thin-walled microstructure shown in Figure 1a. The sample is then immersed in ethanol for development and dries naturally in air after 0.5 h. As the liquid evaporates, a meniscus forms between the microunits when the liquid surface reaches the top of the microstructure, which leads to the generation of capillary force. When the petal bends under the capillary force, an elastic restoring force is generated. If the capillary force exceeds the elastic restoring force, the petals will continue to bend until they are assembled. Once the liquid has completely evaporated, the six petals adhere together to form a 3D microassembly. Finally, the assembly undergoes debinding and sintering to be converted into a transparent silica glass microstructure.

A critical challenge in microscale 4D printing of glass materials lies in matching the driving force (capillary force in this work) with the mechanical properties of the precursor. To address this, a photopolymerizable resin is formulated with an optimized composition of moderate organic cross-linkers and high-loading inorganic silica NPs. The resin is solely composed of methacrylic acid-functionalized silica nanoparticles (MAA-NPs), a photo-cross-linker (poly(ethylene glycol) diacrylate, PEGDA), and a photoinitiator (4,4′-bis(diethylamino)-benzophenone, EMK). The methacrylic acid (MAA) functional groups, which are chemically attached to the silica NPs, enhance the dispersibility of NPs in the resin,[44,46] thereby effectively minimizing light scattering caused by agglomeration during femtosecond laser irradiation. Additionally, the NPs have an average diameter of 21 nm, further contributing to the submicron printing resolution (Figures S1 and S2, Supporting Information). The resin ultimately appears as a clean, transparent, light-yellow solution (Figure S1, Supporting Information). Notably, MAA groups can undergo radical polymerization to achieve the printing of 3D microstructures without the need for additional cross-linkers (Figure S3, Supporting Information). However, in this case, the printed microstructures show limited deformability, as the rigid inorganic particles are tightly packed and occupy most of the space. As demonstrated by in situ compression test, the printed micropillar has a low fracture strain of 12% and a high Young's modulus of 3.58 GPa (Figure S4, Supporting Information). To address this issue, PEGDA is incorporated to enhance the deformability of the polymerized structure. With 15 wt % PEGDA, the printed micropillar exhibits significantly improved mechanical properties. At a laser processing power of 22 mW, the fracture strain reaches 32%, representing a 2.67-fold increase compared to the condition without PEGDA, while the compressive strength remains comparable. The Young's modulus of 1.2 GPa falls within the range typically inducible to deformation by capillary force[57,59] (Figures 1c and S4, Supporting Information). Meanwhile, the silica content within the resin reaches 65 wt % (Figure S5, Supporting Information), which is higher than previously reported 3D-printed glass microstructures (Table S1, Supporting Information) and advantageous for reducing structural shrinkage during sintering. Although further increasing PEGDA content can enhance deformation performance, it reduces silica content

https://doi.org/10.1021/acsnano.5c15343
ACS Nano 2025, 19, 40547−40560

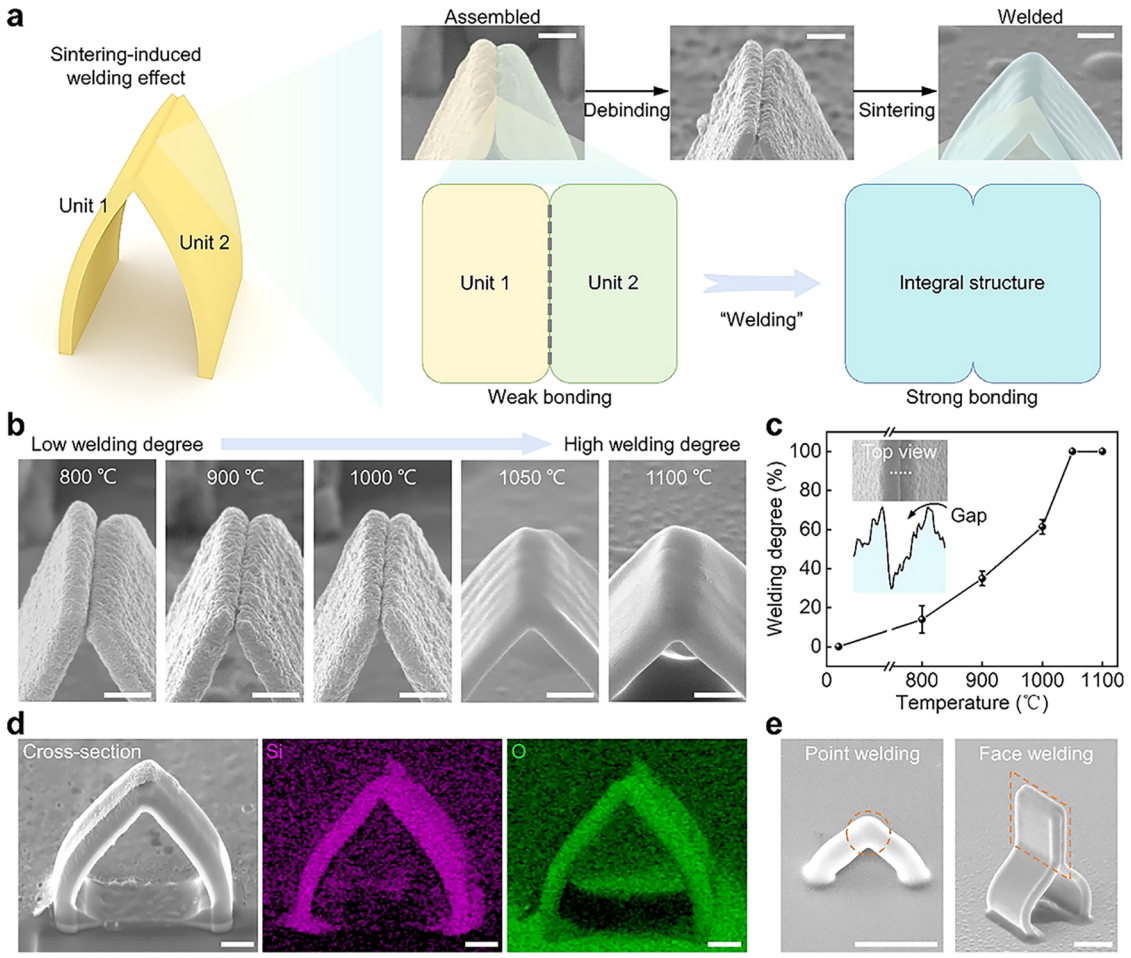

Figure 2. Sintering-induced "welding" effect. (a) Schematic illustration and SEM images of microunits transitioning from weak bonding to strong bonding. Scale bars, 2 μm. (b) SEM images of microassembly sintered at different temperatures demonstrating that welding degree increases with rising sintering temperature. Scale bars, 2 μm. (c) Quantitative changes in welding degree based on the FWHM of gray level profiles across welded interfaces. (d) SEM image and EDS mapping of the FIB-sectioned microassembly validating the welding integrity. Scale bars, 2 μm. (e) Demonstration of point and face welding configurations. Scale bars, 2 μm for the left and 5 μm for the right.

and compromises structural strength, making the assembly unstable under capillary force (Figure S6, Supporting Information). In the final printed microstructure, the NPs and PEGDA are mutually cross-linked, as illustrated in Figure 1a. The printed six-petal thin-walled microstructure exhibits excellent structural integrity and fidelity (Figure S7, Supporting Information).

The assembly of the microunits is governed by the competition between capillary force (F_c) during solvent evaporation and elastic restoring force (F_e) of microunits. The assembly morphology is maintained when the adhesive force (F_a) generated by contact between microunits can counteract the elastic restoring force (Figures 1b and S8 and Movie S1, Supporting Information). As shown in Figure 1d, the six micropetals gather toward the center and form adhesion at the top. The magnitudes of capillary force and elastic restoring force are intrinsically determined by structural parameters and the Young's modulus of the material. Young's modulus exhibits tunability through laser processing power,[70] as higher power enhances cross-linking density, thereby elevating the stiffness of printed structures (Figure 1c). Taking microplate units as an example, by varying geometric dimensions (e.g., the height and thickness of microplates, and the distance between microplates), three distinct assembly states are achieved, including nonassembly, line-contact assembly, and face-contact assembly (Figures S9 and S10, Supporting Information). The laser processing power can be adjusted to regulate the geometric thresholds (the height-to-distance ratio) for successful assembly, as shown in Figure S9, Supporting Information. Low power facilitates assembly by reducing the Young's modulus and elastic restoring force, but excessively low power may cause the collapse of microunits due to insufficient strength to counteract capillary force. Detailed discussions can be found in Note S1, Supporting Information. Additionally, it is worth noting that the microstructure reaches the yield stage between 10% and 16% strain, which indicates that the microstructure undergoes plastic deformation (Figure 1c). The mechanical behavior is attributed to the addition of PEGDA, as this phenomenon is not observed in the material without PEGDA (Figure S4, Supporting Information). Specifically, for nanocomposites with PEGDA added, cavitation induced by filler−matrix interfacial delamination leads to nonrecoverable structural deformation.[71] This plastic behavior gives the microstructure a strain retention rate of 78%, enabling the microstructure to maintain its deformed shape even in the absence of adhesive force (Figure S11, Supporting Information). It should be noted that the plastic deformation only occurs at the high strain stage. In

https://doi.org/10.1021/acsnano.5c15343
ACS Nano 2025, 19, 40547−40560

scenarios involving small strains, elastic deformation remains the dominant form, and the microunits will return to their original upright configuration if assembly is not possible. Moreover, microstructures with identical dimensions exhibit consistent assembly behavior (Figure S12a, Supporting Information), which is attributed to the outstanding stability of MAA-NPs. This is clearly evidenced by the observed stability during the printing process (Movie S2, Supporting Information) and the uniformly distributed silicon elements in the printed structures (Figure S12b,c, Supporting Information).

To be converted into transparent silica glass, the microassembly is subjected to debinding and sintering processes in air (Figure 1a). The debinding process decomposes all organic matter at around 600 °C, which is demonstrated by the thermogravimetric analysis (TGA) (Figure S5, Supporting Information). The sintering process is conducted at a higher temperature to fuse the NPs and promote the densification of the structure. Additional vacuum degreasing steps can be performed before debinding to produce pyrolytic carbon/silica composites to ensure the structural integrity of larger structures during heat treatment[46] (Figure S13, Supporting Information). Owing to the high solid content, the microassembly exhibits a low linear shrinkage, which ensures good structural quality (Figure 1d). The final obtained glass six-petal microassembly has a maximum lateral dimension of 30 × 30 μm and a minimum feature size (wall thickness) of only 800 nm. X-ray photoelectron spectroscopy (XPS) is employed to characterize the composition of the sintered glass. In the full XPS analysis, the elemental composition of the sintered glass aligns with that of commercial fused silica glass (JGS-2 grade, SiO_2 ≥99.9999%), which is mainly composed of silicon and oxygen (Figure 1e and Table S2, Supporting Information). In the fine spectroscopy results, the peaks of the sintered glass match very well with commercial specimens (532.6 eV for O 1s peak, 103.4 eV for Si 2p peak, and 25.3 eV for O 2s peak), which indicates their identical chemical state and structural composition (Figure S14, Supporting Information). The transmission electron microscopy (TEM) image demonstrates the dense nature of the sintered silica glass microstructures, exhibiting an absence of discernible pores or cracks [Figure 1f(i) and (ii)]. The selected area diffraction pattern confirms the amorphous characteristics of the sintered glass [Figure 1f(iii)]. The sintered microstructure exhibits excellent surface quality, with an arithmetic mean line roughness (Ra) of only 2 nm measured by atomic force microscopy (AFM) (Figure S15, Supporting Information). The ultraviolet−visible−near-infrared transmission spectrum shows that the sintered silica glass exhibits exceptional optical transmission properties, achieving over 90% across the entire spectrum (300−1000 nm) without any visible absorption peaks (Figure S16, Supporting Information).

Sintering-Induced Welding Effect. The shape retention force after assembly is adhesive force, which mainly involves van der Waals force in our case. van der Waals force is significantly effective at the microscopic level and is proportional to the contact area. Given the rough surface of the printed microstructure (Figure S17, Supporting Information), the contact area is sufficiently large, which results in a substantial van der Waals force. This force ensures adequate adhesive strength, enabling our assembled structure to maintain its shape perfectly without rebounding during the heating process (Figure S18, Supporting Information). When the debinding process occurs, the microassembly undergoes stress relaxation to form a permanent shape and is subsequently sintered to produce dense silica glass.

The final sintering process not only promotes particle fusion to achieve structural densification but also enhances structural stability beyond the initial assembly configuration. As depicted in Figure 2a, the microunits initially adhere together to form a "metastable" state, where the assembled morphology can be disrupted under specific conditions, such as liquid environments. During heat treatment, the strong sintering forces, driven by the high surface energy of the small-sized NPs, enable fusion bonding between particles at temperatures exceeding 600 °C. This facilitates a transition from weak intermolecular adhesion to strong silicon−oxygen covalent bonding between microunits, resulting in a more robust connection. This phenomenon, where sintering further induces interfacial fusion bonding between microunits to enhance structural integrity and form a unified entity, is defined as "welding" effect. Figure 2b demonstrates the temperature-dependent evolution of the welding degree (w) between microunits, which is defined as

$$w = \frac{g_{T=20} - g_{T=x}}{g_{T=20}} \quad (1)$$

where $g_{T=20}$ and $g_{T=x}$ represent the interfacial gap widths at sintering temperatures of 20 °C and x °C, respectively. These gap widths are determined through grayscale analysis of SEM images, with values corresponding to the full width at half-maximum (FWHM) of gray level profiles across welded interfaces (Figures 2b and S19, Supporting Information). Obviously, w increases progressively with rising sintering temperature, ultimately reaching its maximum value at temperatures above 1050 °C (Figure 2c). To further validate the welding integrity, focused ion beam (FIB) cross-sectioning analysis is conducted on microassemblies sintered at 1050 °C, showing no detectable porosity or interfacial fractures at the welded junctions. EDS elemental mapping demonstrates exceptional compositional uniformity across the welding interface (Figures 2d and S20, Supporting Information). Notably, the welding strategy exhibits multiple connection modes besides line joints, with successful implementation of both point and face welding configurations (Figure 2e). Leveraging the "welding" effects, the resultant microassemblies exhibit enhanced structural stability compared to presintered assemblies, maintaining architectural integrity even under prolonged liquid immersion conditions (Figure S21 and Movie S3, Supporting Information). Furthermore, the deformed and welded glass microassemblies are mechanically robust. In situ compression tests conducted on assemblies with three welding configurations demonstrate excellent compressive resistance (Figure S22, Supporting Information). Microplate assemblies exhibit greater resistance to compressive force compared to micropillar assemblies, which can be attributed to their larger unit size. Face-welded assemblies undergo buckling deformation prior to fracture, thereby enhancing their fracture strain, whereas line-welded structures fracture directly at the base upon reaching their compressive limit. These findings demonstrate the capability of the proposed approach for programming the mechanical properties of the microstructures.

4D-Printed Glass Microassemblies. To demonstrate the robustness of our approach, a variety of 3D glass microassemblies are fabricated. Initial demonstrations focus on three

https://doi.org/10.1021/acsnano.5c15343
ACS Nano 2025, 19, 40547−40560

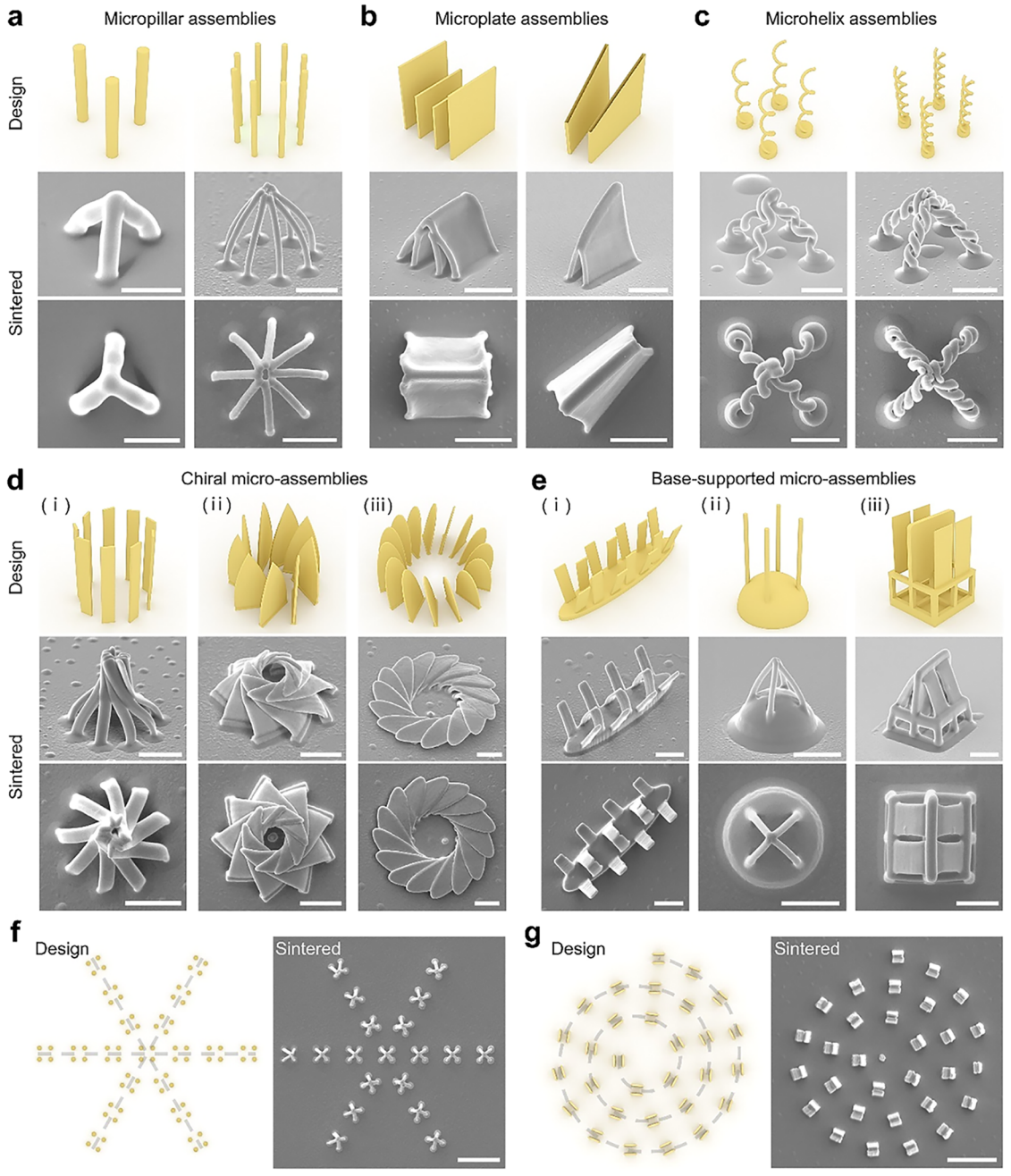

Figure 3. 4D-printed glass microassemblies. (a) Micropillar assemblies with (i) 3 pillars and (ii) 8 pillars. Scale bars, 5 μm for the left and 10 μm for the right. (b) Microplate assemblies with (i) 4 rectangular plates and (ii) 2 trapezoidal plates. Scale bars, 10 μm. (c) Microhelix assemblies with (i) single helices and (ii) double helices. Scale bars, 10 μm. (d) Chiral microassemblies with (i) 9 rectangular plates, (ii) 9 triangle plates, and (iii) 15 tilted plates. Scale bars, 10 μm. (e) Base-supported microassemblies with (i) elliptical base, (ii) hemispherical base and (iii) complex framework base. Scale bars, 10 μm. (f) Micropillar assemblies with radial pattern. Scale bars, 20 μm. (g) Microplate assemblies with spiral pattern. Scale bars, 20 μm.

basic microunit configurations, including micropillar assemblies with tunable numbers and aspect ratios (Figures 3a and S23, Supporting Information), microplate assemblies with tunable numbers and shape (Figure 3b), and microhelix assemblies (Figure 3c). These examples demonstrate the potential of our approach in the fabrication of glass lightguide,[72] cell scaffolds,[68] and microfluidic channels.[62] Building on these, glass chiral microstructures can be produced through asymmetrical capillary force[63] or directional induction method[57,65] (Note S2, Supporting Information). In the first method, microplates with anisotropic rectangular cross section are uniformly distributed along a circular path, with their major axes deviating from the local tangent by a predefined angle β, as shown in Figure S24, Supporting Information. Capillary forces and elastic restoring forces differ significantly between the major and minor axes due to geometric asymmetry, which eventually leads to the creation of spiral assemblies [Figures 3d(i),(ii), and S26a,b, Supporting Information]. Alternatively, the second method introduces out-of-plane tilting angle (α) to induce directional assembly (Figure S25, Supporting Information), forming radially expanding 3D chiral geometries [Figures 3d(iii) and S26c, Supporting Information].

https://doi.org/10.1021/acsnano.5c15343
ACS Nano 2025, 19, 40547−40560

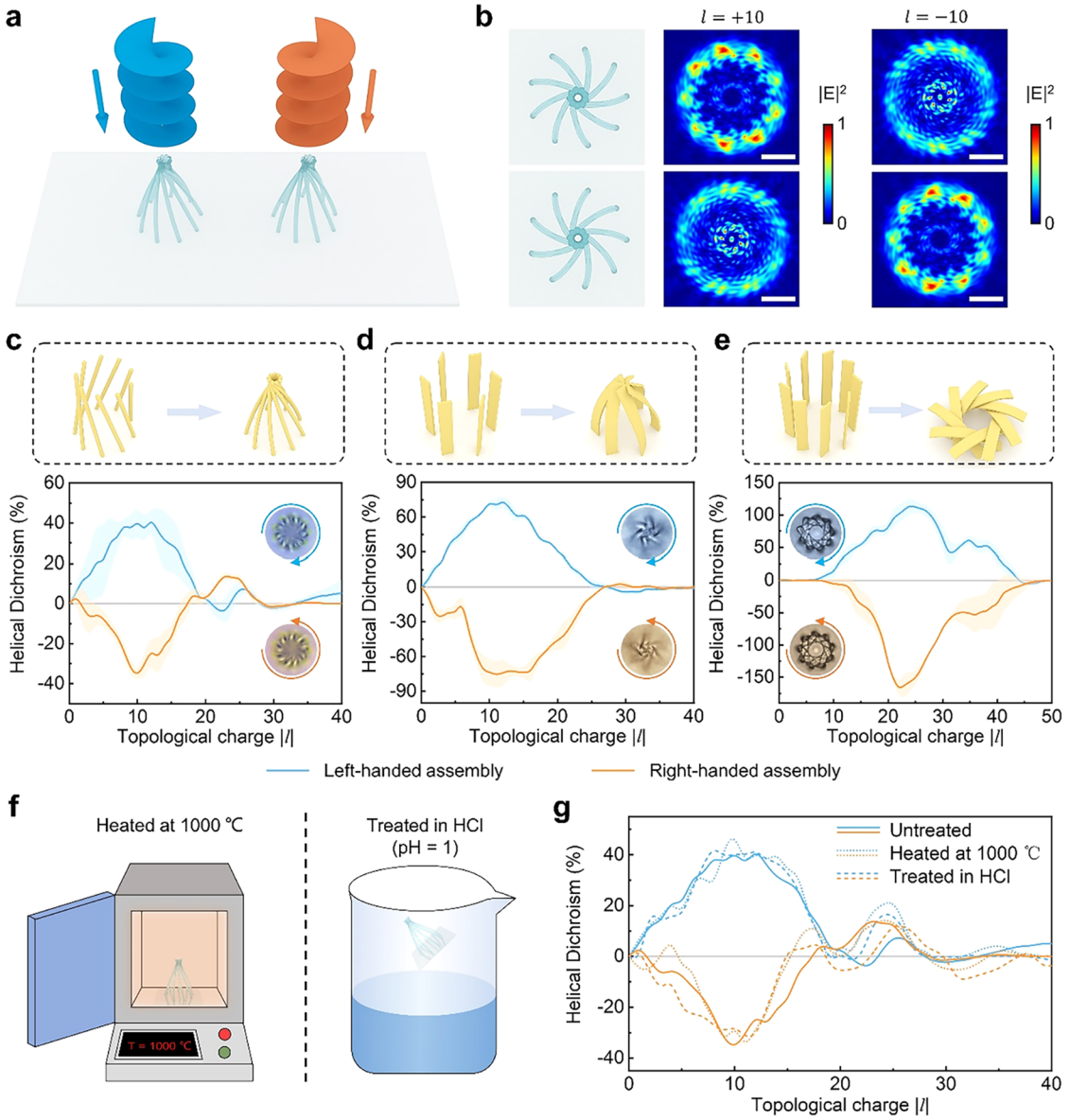

Figure 4. Chiroptical helical dichroism (HD) on glass chiroptical metamaterials. (a) Schematic illustration of the OAM beams irradiating upright onto the chiral microassemblies. (b) Electromagnetic simulations of the 9-micropillar chiral assemblies. Scale bars: 10 μm. (c–e) HD spectra for three distinct glass chiral microassemblies, including (c) 9-micropillar assemblies, (d) 6-microplate assemblies, and (e) 9-microplate assemblies. (f) Schematic illustration of high temperature and HCl treatment for glass chiral microstructures. (g) HD spectra for 9-micropillar chiral assemblies after high temperature and HCl treatment.

It should be noted that the aforementioned structures lack a sacrificial substrate, thus changes in the shape of the assembled structures can be observed during the sintering process. To illustrate this more clearly, we measure the dimensional changes (including the height and width) of a two-microplate assembled structure (arch-shaped) at different sintering temperatures (Figure S27, Supporting Information). Due to the constraint from the substrate, the width at the bottom of the structure (*X*-direction) remains largely unchanged. In contrast, the height (*Z*-direction), being unrestricted, undergoes significant changes. Consequently, the overall structure transform from a tall arch to a shallow arch. This issue can be mitigated by incorporating a sacrificial base, thereby achieving higher fidelity in the assembled structures at the expense of base deformation. Our approach can be applied to fabricate a variety of base-supported microassemblies (Figure 3e). For instance, an elliptical base with alternating vertical and outwardly inclined microplates yields ship-like sintered structures, where inclined microunits fail to assemble under insufficient capillary forces [Figure 3e(i)]. Nonplanar base assembly is demonstrated via 4-micropillar assembly supported by a hemispherical base [Figure 3e(ii)]. Complex framework base is also presented, in which the segmented microplates above are well assembled and welded [Figure 3e(iii)]. Moreover, the spatial position of microassemblies can be easily controlled which leads to diverse ordered patterns, as shown in Figure 3f,g. Overall, these results collectively underscore the adaptability of our approach in the fabrication of complex glass microstructures.

Glass Chiral Microassemblies with Chiroptical Responses. Chiral architectures are ubiquitous in natural systems, exemplified by helical plant tendrils, DNA double

https://doi.org/10.1021/acsnano.5c15343
ACS Nano 2025, 19, 40547–40560

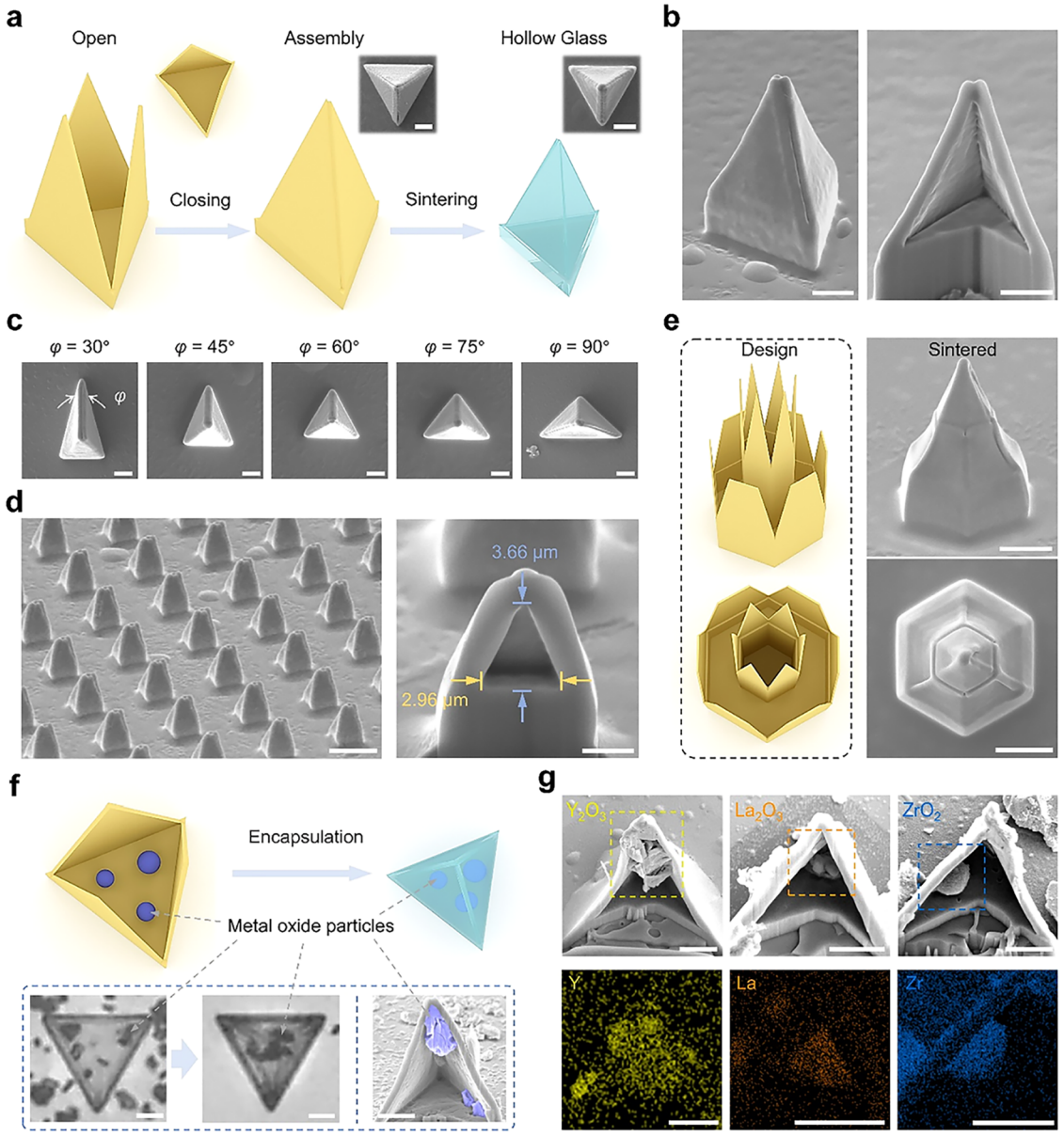

Figure 5. 4D-printed hollow glass microstructures. (a) Schematic illustration of fabricating hollow glass microstructures through the open-assembly process. Scale bars: 5 μm. (b) External and internal SEM images of fabricated hollow glass microstructures. Scale bars: 5 μm. (c) Hollow glass microstructures with varying apex angle φ of the base triangle. Scale bars: 5 μm. (d) The smallest hollow pentahedron. Scale bars: 10 μm for the left and 2 μm for the right. (e) Multilayer hollow structures. Scale bars: 10 μm. (f) The "encapsulation" process for metal oxide particles. Scale bars: 5 μm. (g) EDS mapping of encapsulated yttrium, lanthanum, and zirconium oxides. Scale bars: 5 μm.

helices, and drug molecules. Recent studies have demonstrated that artificially constructed 3D chiral microstructures hold critical significance in investigating chiral light-matter interactions.[73,74] Their 3D configuration greatly enhances chiroptical responses, thereby unlocking transformative potential for applications in chiroptical sensing[75] and chiral molecules detection.[76] Capillary-force-assisted assembly offers a cost-efficient and scalable approach for creating chiral microstructures;[63−67] however, current implementations predominantly employ organic or organic−inorganic hybrid materials that show limited stability under thermal or liquid conditions.[77] Silica glass addresses these limitations through its thermal stability, chemical durability, and biocompatibility, which makes it an ideal choice for chiral microstructure construction. Moreover, due to the welding effect, the silica chiral microassemblies fabricated by our approach exhibit exceptional stability even in liquid environments, which further expands the range of applicable environments.

Optical vortices carrying orbital angular momentum (OAM) provide an effective way to detect optical chirality in microscopic objects.[63,76] The reflectance difference of chiral microstructures under incident vortex beams with opposite OAM modes can be observed, which is defined as helical dichroism (HD). As illustrated in Figure 4a, HD measurement is conducted by vertically illuminating the chiral microassemblies with vortex beams of different topological charges. Detailed procedures and the measurement setup can be found in the Experimental Section and Figure S28, Supporting Information. Electromagnetic field simulations for vortex beams with topological charge $l = \pm 10$ show chirality-

https://doi.org/10.1021/acsnano.5c15343
ACS Nano 2025, 19, 40547−40560

dependent electric field distributions, confirming chiroptical responses (Figure 4b). We measure the HD spectra of three distinct chiral microassemblies, including 9-micropillar assemblies, 6-microplate assemblies, and 9-microplate assemblies (Figures 4c,d and S29, Supporting Information). The 9-micropillar assemblies are fabricated via the aforementioned directional induction method, while the 6- and 9-microplate assemblies are produced using asymmetric capillary force-based approach (Note S2 and Figure S30, Supporting Information). Among these, the 9-microplate assemblies exhibit inhibited central convergence when compared to the 9-microplate assembly in Figure 3d(i) due to the increased β. Instead, it forms support preferentially within the midregion rather than the upper region, resulting in a centrally voided architecture (Figure S31, Supporting Information). Experimental HD spectra of these silica chiral microassemblies all exhibit giant chiroptical HD signals and near-mirror symmetry between opposite chiral structures, verifying fabrication reliability (Figure 4c,d). Minor symmetry deviations arise from nonuniform beam energy distribution and imperfect structural mirror symmetry. HD peak positions vary with microstructure size, and larger structures require higher topological charges for peak responses. Microplate chiral assembly exhibits higher HD response compared to micropillar chiral assembly. Notably, the HD spectra of the 9-microplate assemblies show zero low-l chiroptical signals, which originates from the central void geometric characteristics. Using our approach, it is expected to create more diverse chiral microstructures with giant chiroptical responses.

Furthermore, to demonstrate the stability of the glass chiral microassembly, it is subjected to a high-temperature environment at 1000 °C for 1 h and immersed in hydrochloric acid (HCl) for 10 h (Figure 4f). The HD spectra of 9-micropillar chiral assemblies after treatment almost overlap, which demonstrates that the chiral microassemblies have not been damaged (Figure 4g). These examples demonstrate the potential of our approach to generate glass chiral metamaterials with giant chiroptical responses and robust stability, which have broad application prospects in chiroptical sensing and biomolecular detection.

Hollow Glass Microstructures for Inorganic Particle Encapsulation. Hollow glass microstructures exhibit excellent application prospects in fields such as light manipulation, solar modules,[78] and thermal insulation.[79] To our best knowledge, there is currently no method capable of directly fabricating hollow microstructures using conventional photopolymerization-based additive manufacturing techniques. This is because the printed structures require a development step to remove unpolymerized parts, and the central hollow region, which the developer cannot access, cannot be effectively removed, ultimately resulting in the formation of a solid structure. Our 4D printing solution overcomes this challenge through the open-assembly process. As shown in Figure 5a, the initial printed microstructure consists of three triangular microplates arranged in a triangular configuration and a base. Due to their open state, the unpolymerized materials in the central region are easily dissolved in the developer. Capillary forces then drive structural closure into a tetrahedral configuration. Minor gaps caused by fabrication tolerances are eliminated by welding during sintering, producing fully enclosed hollow glass microstructures. FIB cross-section analysis confirms complete edge welding and the absence of internal residues (Figure 5b). Hollow microstructure dimensions can be precisely controlled by adjusting structural parameters, such as base dimensions and microplate height (Figure S32, Supporting Information), the apex angle φ of the base triangle (Figure 5c), and the number of microplates (Figure S33, Supporting Information). Our approach successfully achieves a smallest hollow pentahedron with 2.96 μm base edge length, 3.66 μm height, and 10.69 μm^3 volume (Figure 5d), while maintaining excellent uniformity (Figure S34, Supporting Information). A multilayer hollow microstructure is further demonstrated, confirming the flexibility of our approach (Figure 5e).

These hollow glass microassemblies enable novel applications in the micronanomanufacturing field, such as inorganic particle encapsulation. As a proof of concept, we successfully encapsulate yttrium, lanthanum, and zirconium oxides into hollow glass microstructures. During the process, metal oxide particles are mixed with the developer and settled into the open structure under gravity. Subsequent assembly and sintering weld the structure, completing the "encapsulation" process (Figure 5f and Movie S4, Supporting Information). FIB-sectioned samples with EDS mapping confirm successful encapsulation (Figures 5g and S35, Supporting Information). Besides the demonstrated encapsulation of yttrium, lanthanum, and zirconium oxides, the 4D printing approach can be readily extended to a broad library of functional metal and alloy particles. These encapsulated microstructures are expected to serve as protective shells for fluorescent[80] and cytotoxic particles,[81,82] showing promising potential in optical sensing and biomedical applications. Moreover, our approach facilitates the fabrication of semienclosed microfluidic channels (Figure S36 and Movie S5, Supporting Information). Compared to conventional TPP-printed microchannels requiring prolonged development times (limited solvent access through narrow openings), the open-assembly approach enables rapid removal of unpolymerized resin, which significantly reduces development time (Figure S37, Supporting Information).

CONCLUSION

In this work, we present a capillary-based 4D printing approach to induce the programmable and precise deformation of glass precursors, which are subsequently converted into fused silica glass microstructures. Through tailored mechanics of TPP-printed precursors and postprint capillary-driven assembly, the approach enables fabrication of intricate 3D glass microarchitectures with submicron resolution that previously pose significant fabrication challenges. This work establishes a foundational pathway for micro/nanoscale glass 4D printing by elucidating key mechanisms that govern the transformation from printed precursors to stable functional devices, such as capillary-force-driven reconfiguration and sintering-induced welding. The fully enclosed hollow microarchitectures exemplify fabrication capabilities beyond the reach of conventional TPP, while the chiroptical metamaterials showcase giant optical responses and superior environmental robustness compared to polymeric counterparts. It should be noted that due to the inherent hardness and brittleness of inorganic materials, direct room-temperature deformation of glass remains highly challenging. Therefore, the shape morphing in this work is achieved in the polymer-inorganic precursor state, which is consistent with most current 4D printing strategies for inorganic materials. This decoupling of the shaping step from the material finalization step provides a viable pathway to circumvent the inherent limitations of 4D printing hard and

https://doi.org/10.1021/acsnano.5c15343
ACS Nano 2025, 19, 40547−40560

brittle inorganic materials. Overall, this work not only establishes a scalable platform for high-precision glass microfabrication but also deepens the understanding of material-structure−property relationships in inorganic 4D printing, which is expected to be applied to a broader class of functional microsystems.

EXPERIMENTAL SECTION

Materials and Resin Preparation. A solution of propylene glycol monomethyl ether containing homogeneously dispersed MAA-functionalized colloidal silica NPs (SiO_2 content ∼40 wt %) is purchased from Shanghai Jiute Nanomaterial Technology Co., Ltd. Poly(ethylene glycol) diacrylate (PEGDA, average molecular weight ∼700, containing 100−300 ppm BHT stabilizer) and Phenylbis (2,4,6-trimethylbenzoyl) phosphine oxide (XBPO, 98%) are purchased from Macklin. 4,4′-Bis(diethylamino)benzophenone (EMK, ≥99%) is purchased from Aladdin. Ethanol (≥99.5%) is purchased from Sinopharm Chemical Reagent Co., Ltd. Sapphire wafer (20 × 20 × 0.2 mm) is purchased from Donghai County Liusha Optoelectronic Technology Co., Ltd. Yttrium, lanthanum, and zirconium oxides are purchased from Nangong Jiannuo Trading Co., Ltd.

For silica-based resin preparation, 0.5 g of PEGDA and 7 g of colloidal silica solution are mixed together by vortex oscillation for 30 s, followed by ultrasonic concussion until bubbles disappear. Then, the mixture is kept in an oven at 110 °C for 7 h to totally evaporate the solvent. At last, 40 mg of EMK is added to the mixture. The mixture is sonicated until the resulting solution becomes totally transparent. For bulk samples, 20 mg of XBPO is added to cure the samples using an ultraviolet light source.

TPP Printing, Capillary-Force-Assisted Assembly, and Heat Treatment Processes. The femtosecond laser source is a mode-locked Ti:sapphire ultrafast oscillator (Chameleon Vision-S, Coherent) with a central wavelength of 800 nm. The pulse width is 75 fs, and the repetition rate is 80 MHz. The laser is tightly focused using a 60× oil objective with high numerical aperture (NA = 1.35) in order to realize high resolution. The laser focus is steered by a pair of galvo-mirrors for 2D scanning, while the step between two layers is realized by linear nanopositioning. In the experiment, the silica nanocomposite is placed in the interlayer between the substrate (sapphire wafer, 200 μm) and the thin glass slide (170 μm). The interlayer is separated by Kapton tape with a thickness of 120 μm. Point-by-point scanning paths are generated from homemade slicing software. The laser power and scanning speed are set to 22 mW and 200 μm s^{-1}, respectively. Finally, the processed sample is immersed in a developing solution (ethanol) for 30 min to remove the uncured precursor.

The developed sample is placed in air at the ambient temperature or on a hot plate at 100 °C for rapid evaporation. The microunits are assembled into a variety of 3D microarchitectures induced by capillary force generated by the evaporation of the liquid remaining between neighboring microunits.

Heat treatment is divided into debinding and sintering, which are performed in a muffle furnace (HF-kejing KSL-1500X, China) in air. The heating procedure: (i) 1 °C min^{-1}, from room temperature to 200 °C, keep for 2 h; (ii) 1 °C min^{-1}, from 200 to 400 °C, keep for 3 h; (iii) 1 °C min^{-1}, from 400 to 600 °C, keep for 2 h; (iv) 1 °C min^{-1}, from 600 to 1050 °C, keep for 30 min; (v) 3 °C min^{-1}, from 1050 °C to room temperature. Additional vacuum degreasing steps can be performed before debinding to produce pyrolytic carbon/silica composites to ensure the structural integrity of larger structures during heat treatment. The process is undertaken in a tube furnace (HF-kejing OTF-1200X, China) in a vacuum with a pressure of −0.1 MPa. The heating procedure: (i) 1 °C min^{-1}, from room temperature to 300 °C, keep for 2 h; (ii) 1 °C min^{-1}, from 300 to 550 °C, keep for 3 h; (iii) 3 °C min^{-1}, from 550 °C to room temperature. Illustrated heating procedures are plotted in Figure S12, Supporting Information.

Measurement and Simulations of Helical Dichroism. The optical vortices are generated by a spatial light modulator (SLM, Pluto NIR-II, Holoeye Photonics). This liquid-crystal SLM working on a reflective mode featured 1920 × 1080 resolution, 8 μm pixel pitch, on which programmable computer-generated holograms (CGHs) with 256 gray levels can be encoded to generate optical vortices with different topological charges (Figure S24, Supporting Information). In order to separate the unwanted zero-order beams from the optical vortices, superposition of a blazed grating is performed. The monochromic light source is the same as that in the fabrication system, with a wavelength of 800 nm and a laser power of 0.5 mW is used for characterization. After aligning the center of the optical vortex to the chiral microstructure, the reflected intensity profiles are captured by a charge-coupled device (CCD) camera (WV-BP334, Panasonic). The collected data is analyzed using numerical computation software. HD is calculated using the following formula:

$$\mathrm{HD} = 2 \times \frac{I_{+l} - I_{-l}}{I_{+l(\max)} + I_{-l(\max)}} \times 100\% \tag{2}$$

where I_{+l} and I_{-l} represent reflected intensities under $+l$ and $-l$ vortex illumination, respectively. Meanwhile, the terms $I_{+l(\max)}$ or $I_{-l(\max)}$ denote the maximum reflection intensity obtained as the topological charge l varies, effectively normalizing the differential signal.

The reflection numerical simulation is carried out using finite difference software based on the time domain (Lumerical FDTD Solutions). In the simulation, the FDTD script function is used to establish the chiral structure model, which is consistent with the actual processing structure. Perfectly matched layer boundaries are applied for the X, Y, and Z directions, and the minimum mesh step is set to be 100 nm.

Characterization. The SEM images are collected with a secondary-electron scanning electron microscopy (EVO18, ZEISS) operated at an accelerating voltage of 10 kV after depositing ∼10 nm gold. TEM images of the NPs are obtained by high-resolution transmission electron microscopy (HT7700 Exalens, HITACHI) at an operating acceleration voltage of 200 kV. TEM characterizations of sintered glass are done with a field emission transmission electron microscope (JEM-2100F, JEOL) at an operating acceleration voltage of 200 kV. The tested TEM samples are sliced from sintered silica glass microstructures via focused ion beam (FIB, FEI Helios NanoLab650, Thermo Fisher Scientific) cutting. Optical microscopy images are obtained using an inverted microscope (DMI 3000B, Leica). TGA data is collected using an STA 8000-HpQ 20QIC at a heating rate of 10 to 1200 °C under air atmosphere. The tested sample is obtained through UV curing. FTIR spectra are obtained using a Fourier transform infrared spectrometer (Thermo Nicolet iS5, Thermo Fisher Scientific). X-ray photoelectron spectra (XPS) are analyzed using an in situ X-ray photoelectron spectrometer (ESCALAB 250Xi, Thermo Fisher Scientific). The surface roughness is measured using an AFM (Dimension Icon, Bruker). Optical transmission is characterized using an UV−vis−NIR spectrometer (SolidSpec-3700i, Shimadzu). The tested sample is obtained through UV curing and sintering to meet the testing requirements for sample area. The EDS analysis spectroscopy images are obtained on a Schottky field emission scanning electron microscope (Gemini SEM 500, ZEISS). The in situ compression tests of the micropillar are conducted by KLA NanoFlip Nanoindenter with a diamond flat punch tip with a diameter of 10 μm inside a ZEISS Gemini SEM 360. The compression tests are performed at a displacement rate of 10 nm s^{-1}. The force signal is acquired through a pressure transducer.

ASSOCIATED CONTENT

Supporting Information

The Supporting Information is available free of charge. (PDF)
The Supporting Information is available free of charge at https://pubs.acs.org/doi/10.1021/acsnano.5c15343.

Supplementary notes; size characterization of silica nanoparticles; evaluation of the print resolution of the resin; photopolymerization without cross-linkers; mechanical behavior of the printed micropillars with different contents of PEGDA; TGA result of the resin; demonstration of microplate assembly with different

https://doi.org/10.1021/acsnano.5c15343
ACS Nano 2025, 19, 40547−40560

contents of PEGDA; design and SEM image of printed six-petal thin-walled microstructure; dimensional parameters of microplates assembly; varieties of assembly states with tunable microplate structural parameters and laser power; SEM images of microplate assembly with 22 mW laser power; plastic behavior of the printed microstructures; stability assessment of nanoparticles; heating procedure for postprocessing; fine XPS spectra of elemental lines of sintered glass compared to commercial fused silica glass; surface roughness measurements of the sintered glass; ultraviolet−visible−near-infrared transmission spectrum of a sintered silica glass monolith with a thickness of 200 μm; AFM measurements on the printed microstructure; optical images of microplate assemblies during heating process; grayscale analysis of SEM images of microplate assemblies with different sintering temperatures; FIB cross-sectioning analysis on assemblies sintered at 1050 °C; comparison of stability in liquid between presintered assemblies and welded assemblies; mechanical behavior of the glass assemblies; micropillar assemblies with tunable numbers; chiral microassemblies based on asymmetrical capillary force method; chiral microassemblies based on directional induction method; design schematic diagram of three chiral microassemblies; dimensional changes of microplate assembly structures at different sintering temperatures; experimental apparatus utilized for the tailorable VD experiment; measured reflection intensity on left-handed and right-handed chiral microstructures illuminated by optical vortices with different topological charges; design schematic diagram of three chiral microassemblies for HD measurement; 9-microplate assembly with increased β; hollow microstructure dimensions controlled by base dimensions and microplate heights; hollow microstructure dimensions controlled by the number of microplates; FIB cross-sectioning analysis on hollow pentahedron; FIB-sectioned samples with EDS mapping confirming successful encapsulation of yttrium, lanthanum, and zirconium oxides; micro-4D-printed glass microchannel; comparison of development time between conventional direct TPP printing and our strategy; the comparison of silica content; the elemental composition analyzed from the XPS results of printed, sintered, and commercial samples (PDF)

Assembly of microplates (MP4)

Printing process (MP4)

Comparison of stability in liquid between presintered assemblies and welded assemblies (MP4)

Encapsulation of metal oxide particles (MP4)

Liquid flowing in glass microchannels (MP4)

AUTHOR INFORMATION

Corresponding Authors

Yanlei Hu − *CAS Key Laboratory of Mechanical Behavior and Design of Materials, Key Laboratory of Precision Scientific Instrumentation of Anhui Higher Education Institutes, Department of Precision Machinery and Precision Instrumentation, University of Science and Technology of China, Hefei 230027, China;* orcid.org/0000-0003-1964-0043; Email: huyl@ustc.edu.cn

Jiawen Li − *CAS Key Laboratory of Mechanical Behavior and Design of Materials, Key Laboratory of Precision Scientific Instrumentation of Anhui Higher Education Institutes, Department of Precision Machinery and Precision Instrumentation, University of Science and Technology of China, Hefei 230027, China;* orcid.org/0000-0003-3950-6212; Email: jwl@ustc.edu.cn

Authors

Yuan Tao − *CAS Key Laboratory of Mechanical Behavior and Design of Materials, Key Laboratory of Precision Scientific Instrumentation of Anhui Higher Education Institutes, Department of Precision Machinery and Precision Instrumentation, University of Science and Technology of China, Hefei 230027, China*

Rui Li − *Institute of Nanotechnology, Karlsruhe Institute of Technology, Karlsruhe 76131, Germany*

Zhaoxin Lao − *Anhui Province Key Laboratory of Measuring Theory and Precision Instrument, School of Instrument Science and Optoelectronics Engineering, Hefei University of Technology, Hefei 230009, China;* orcid.org/0000-0002-7673-0590

Yusheng Jin − *CAS Key Laboratory of Mechanical Behavior and Design of Materials, Key Laboratory of Precision Scientific Instrumentation of Anhui Higher Education Institutes, Department of Precision Machinery and Precision Instrumentation, University of Science and Technology of China, Hefei 230027, China*

Hao Wu − *School of Microelectronics, Hefei University of Technology, Hefei 230601, China*

Zeheng Wu − *CAS Key Laboratory of Mechanical Behavior and Design of Materials, Key Laboratory of Precision Scientific Instrumentation of Anhui Higher Education Institutes, Department of Precision Machinery and Precision Instrumentation, University of Science and Technology of China, Hefei 230027, China*

Wei Zeng − *CAS Key Laboratory of Mechanical Behavior and Design of Materials, Key Laboratory of Precision Scientific Instrumentation of Anhui Higher Education Institutes, Department of Precision Machinery and Precision Instrumentation, University of Science and Technology of China, Hefei 230027, China*

Modong Jiang − *CAS Key Laboratory of Mechanical Behavior and Design of Materials, Key Laboratory of Precision Scientific Instrumentation of Anhui Higher Education Institutes, Department of Precision Machinery and Precision Instrumentation, University of Science and Technology of China, Hefei 230027, China*

Jincheng Ni − *CAS Key Laboratory of Mechanical Behavior and Design of Materials, Key Laboratory of Precision Scientific Instrumentation of Anhui Higher Education Institutes, Department of Precision Machinery and Precision Instrumentation, University of Science and Technology of China, Hefei 230027, China*

Dong Wu − *CAS Key Laboratory of Mechanical Behavior and Design of Materials, Key Laboratory of Precision Scientific Instrumentation of Anhui Higher Education Institutes, Department of Precision Machinery and Precision Instrumentation, University of Science and Technology of China, Hefei 230027, China;* orcid.org/0000-0003-0623-1515

Jiaru Chu − *CAS Key Laboratory of Mechanical Behavior and Design of Materials, Key Laboratory of Precision Scientific*

https://doi.org/10.1021/acsnano.5c15343
ACS Nano 2025, 19, 40547−40560

Instrumentation of Anhui Higher Education Institutes, Department of Precision Machinery and Precision Instrumentation, University of Science and Technology of China, Hefei 230027, China; orcid.org/0000-0001-6472-8103

Complete contact information is available at: https://pubs.acs.org/10.1021/acsnano.5c15343

Author Contributions

[⊥]The manuscript was written through contributions of all authors. All authors have given approval to the final version of the manuscript. Y.T. and R.L. contributed equally to this work.

Notes

The authors declare no competing financial interest.

ACKNOWLEDGMENTS

This work was supported by the National Key Research and Development Program of China (No. 2021YFF0502700, 2024YFB4610700), the National Natural Science Foundation of China (Nos. 52075516, 62325507, 52175396, 62375253, 52375582, 62405307), Major Scientific and Technological Projects in Anhui Province (202103a05020005, 202203a05020014), Anhui Provincial Natural Science Foundation (2308085QF218), Hefei Municipal Natural Science Foundation (No. HZR2450), the Independent Deployment Project of HFNL (Grant No. ZB2025010600), the Fundamental Research Funds for the Central Universities (WK2090050048), Xiaomi Young Scholars Program, and the Students' Innovation and Entrepreneurship Foundation of USTC (CY2024G003B, CY2024G017A, CY2024C002A). We acknowledge the Experimental Center of Engineering and Material Sciences at USTC for the fabrication and measurement of samples. This work was partially carried out at the USTC Center for Micro and Nanoscale Research and Fabrication and Instruments Center for Physical Science, University of Science and Technology of China.

REFERENCES

(1) Ding, A. X.; Tang, F.; Alsberg, E. 4D Printing: A Comprehensive Review of Technologies, Materials, Stimuli, Design, and Emerging Applications. *Chem. Rev.* **2025**, *125* (7), 3663−3771.

(2) Ding, A. X.; Tang, F.; Alsberg, E. The Emerging 4D Printing of Shape-Memory Thermomorphs for Self-Adaptative Biomedical Implants. *Adv. Funct. Mater.* **2025**, *35* (28), No. 202418348.

(3) Zhang, B.; Li, H. G.; Cheng, J. X.; Ye, H. T.; Sakhaei, A. H.; Yuan, C.; Rao, P.; Zhang, Y. F.; Chen, Z.; Wang, R.; He, X. N.; Liu, J.; Xiao, R.; Qu, S. X.; Ge, Q. Mechanically Robust and UV-Curable Shape-Memory Polymers for Digital Light Processing Based 4D Printing. *Adv. Mater.* **2021**, *33* (27), No. 2101298.

(4) Yue, L.; Sun, X. H.; Yu, L. X.; Li, M. Z.; Montgomery, S. M.; Song, Y. Y.; Nomura, T.; Tanaka, M.; Qi, H. J. Cold-Programmed Shape-Morphing Structures Based on Grayscale Digital Light Processing 4D Printing. *Nat. Commun.* **2023**, *14* (1), No. 5519.

(5) Shi, Y. P.; Fang, G. Q.; Cao, Z. L.; Shi, F. Z.; Zhao, Q.; Fang, Z. Z.; Xie, T. Digital Light Fabrication of Reversible Shape Memory Polymers. *Chem. Eng. J.* **2021**, *426*, No. 131306.

(6) Tang, T. T.; Alfarhan, S.; Jin, K. L.; Li, X. J. 4D Printing of Seed Capsule-Inspired Hygro-Responsive Structures Via Liquid Crystal Templating-Assisted Vat Photopolymerization. *Adv. Funct. Mater.* **2023**, *33* (5), No. 2211602.

(7) Cecchini, L.; Mariani, S.; Ronzan, M.; Mondini, A.; Pugno, N. M.; Mazzolai, B. 4D Printing of Humidity-Driven Seed Inspired Soft Robots. *Adv. Sci.* **2023**, *10* (9), No. 2205146.

(8) Cheng, T.; Thielen, M.; Poppinga, S.; Tahouni, Y.; Wood, D.; Steinberg, T.; Menges, A.; Speck, T. Bio-Inspired Motion Mechanisms: Computational Design and Material Programming of Self-Adjusting 4D-Printed Wearable Systems. *Adv. Sci.* **2021**, *8* (13), No. 2100411.

(9) Münchinger, A.; Hahn, V.; Beutel, D.; Woska, S.; Monti, J.; Rockstuhl, C.; Blasco, E.; Wegener, M. Multi-Photon 4D Printing of Complex Liquid Crystalline Microstructures by in Situ Alignment Using Electric Fields. *Adv. Mater. Technol.* **2025**, *12* (1), No. 2100944.

(10) Lugger, S. J. D.; Ceamanos, L.; Mulder, D. J.; Sanchez-Somolinos, C.; Schenning, A. P. H. J. 4D Printing of Supramolecular Liquid Crystal Elastomer Actuators Fueled by Light. *Adv. Mater. Technol.* **2023**, *8* (5), No. 2201472.

(11) Deng, C. S.; Liu, Y. C.; Fan, X. H.; Jiao, B. Z.; Zhang, Z. X.; Zhang, M. D.; Chen, F. Y.; Gao, H.; Deng, L. M.; Xiong, W. Femtosecond Laser 4D Printing of Light-Driven Intelligent Micromachines. *Adv. Funct. Mater.* **2023**, *33* (11), No. 2211473.

(12) Ding, A.; Cleveland, D. S.; Gasvoda, K. L.; Alsberg, E. Cell Contractile Forces Drive Spatiotemporal Morphogenesis in 4D Bioprinted Living Constructs. *Matter* **2025**, *8*, No. 102413, DOI: 10.1016/j.matt.2025.102413.

(13) Xu, S.; Yan, Z.; Jang, K. I.; Huang, W.; Fu, H. R.; Kim, J.; Wei, Z.; Flavin, M.; McCracken, J.; Wang, R.; Badea, A.; Liu, Y.; Xiao, D. Q.; Zhou, G. Y.; Lee, J.; Chung, H. U.; Cheng, H. Y.; Ren, W.; Banks, A.; Li, X. L.; et al. Assembly of Micro/Nanomaterials into Complex, Three-Dimensional Architectures by Compressive Buckling. *Science* **2015**, *347* (6218), 154−159.

(14) Cheng, X.; Fan, Z. C.; Yao, S. L.; Jin, T. Q.; Lv, Z. Y.; Lan, Y.; Bo, R. H.; Chen, Y. T.; Zhang, F.; Shen, Z. M.; Wan, H. H.; Huang, Y. G.; Zhang, Y. H. Programming 3D Curved Mesosurfaces Using Microlattice Designs. *Science* **2023**, *379* (6638), 1225−1232.

(15) Wan, X.; Xiao, Z. M.; Tian, Y. J.; Chen, M.; Liu, F.; Wang, D.; Liu, Y.; Bartolo, P. J. D.; Yan, C. Z.; Shi, Y. S.; Zhao, R. R.; Qi, H. J.; Zhou, K. Recent Advances in 4D Printing of Advanced Materials and Structures for Functional Applications. *Adv. Mater.* **2024**, *36* (34), No. 2312263.

(16) Xu, X.; Wang, Y. X.; Liu, D. S.; Yang, X. X.; Lu, Y. Z.; Jiang, P.; Wang, X. L. Sophisticated Structural Ceramics Shaped from 3D Printed Hydrogel Preceramic Skeleton. *Adv. Mater.* **2024**, *36* (33), No. 2404469.

(17) Jian, B. C.; Demoly, F.; Zhang, Y. C.; Qi, H. J.; André, J. C.; Gomes, S. Origami-Based Design for 4D Printing of 3D Support-Free Hollow Structures. *Engineering* **2022**, *12*, 70−82.

(18) Huang, T. Y.; Huang, H. W.; Jin, D. D.; Chen, Q. Y.; Huang, J. Y.; Zhang, L.; Duan, H. L. Four-Dimensional Micro-Building Blocks. *Sci. Adv.* **2020**, *6* (3), No. eaav8219.

(19) Hu, Y. L.; Wang, Z. Y.; Jin, D. D.; Zhang, C. C.; Sun, R.; Li, Z. Q.; Hu, K.; Ni, J. C.; Cai, Z.; Pan, D.; Wang, X. W.; Zhu, W. L.; Li, J. W.; Wu, D.; Zhang, L.; Chu, J. R. Botanical-Inspired 4D Printing of Hydrogel at the Microscale. *Adv. Funct. Mater.* **2020**, *30* (4), No. 1907377.

(20) Zhang, W.; Wang, H.; Wang, H. T.; Chan, J. Y. E.; Liu, H. L.; Zhang, B. A.; Zhang, Y. F.; Agarwal, K.; Yang, X. L.; Ranganath, A. S.; Low, H. Y.; Ge, Q.; Yang, J. K. W. Structural Multi-Colour Invisible Inks with Submicron 4D Printing of Shape Memory Polymers. *Nat. Commun.* **2021**, *12* (1), No. 112.

(21) Wang, R.; Yuan, C.; Cheng, J. X.; He, X. N.; Ye, H. T.; Jian, B. C.; Li, H. G.; Bai, J. M.; Ge, Q. Direct 4D Printing of Ceramics Driven by Hydrogel Dehydration. *Nat. Commun.* **2024**, *15* (1), No. 758.

(22) Liu, G.; Zhang, X. F.; Lu, X. Y.; Zhao, Y.; Zhou, Z. F.; Xu, J. J.; Yin, J. A.; Tang, T.; Wang, P. Y.; Yi, S. H.; Fan, J. F.; Zhuo, X. S.; Chan, Y. H.; Wong, W. L.; Bian, H. D.; Zuo, J.; Dai, Y.; Wu, J.; Lu, J. 4D Additive-Subtractive Manufacturing of Shape Memory Ceramics. *Adv. Mater.* **2023**, *35* (39), No. 2302108.

(23) Bargardi, F. L.; Le Ferrand, H.; Libanori, R.; Studart, A. R. Bio-Inspired Self-Shaping Ceramics. *Nat. Commun.* **2016**, *7*, No. 13912.

(24) Ding, Z. Z.; Zreiqat, H.; Mirkhalaf, M. Rationally-Designed Self-Shaped Ceramics through Heterogeneous Green Body Compositions. *Mater. Horiz.* **2022**, *9* (11), 2762−2772.

(25) Wan, L.; Mao, Z. Y.; Liu, H.; Xie, Y. E.; Lyu, F. C.; Cao, Z. W. B.; He, Y. H.; Yin, J. N.; Han, X. Q.; Chan, W. Y. K.; Lu, J. Direct 4D Printing of Gradient Structure of Ceramics. *Chem. Eng. J.* **2023**, *465*, No. 142804.
(26) Wang, F.; Liu, C. C.; Yang, H. T.; Wang, H.; Zhang, H.; Zeng, X. X.; Wang, C.; Zhang, W. Z.; Lv, W. J.; Zhu, P. F.; Li, B. 4D Printing of Ceramic Structures. *Addit. Manuf.* **2023**, *63*, No. 103411.
(27) Liu, G.; Zhao, Y.; Wu, G.; Lu, J. Origami and 4D Printing of Elastomer-Derived Ceramic Structures. *Sci. Adv.* **2018**, *4* (8), No. eaat0641.
(28) Zheng, N.; Hou, J. J.; Zhao, H. B.; Wu, J. J.; Luo, Y. W.; Bai, H.; Rogers, J. A.; Zhao, Q.; Xie, T. Mechano-Plastic Pyrolysis of Dynamic Covalent Polymer Network toward Hierarchical 3D Ceramics. *Adv. Mater.* **2019**, *31* (11), No. 1807326.
(29) Huang, K.; Elsayed, H.; Franchin, G.; Colombo, P. Complex Sioc Ceramics from 2D Structures by 3D Printing and Origami. *Addit. Manuf.* **2020**, *33*, No. 101144.
(30) Shan, Y.; Liu, S. Y.; Wang, B.; Hong, Y.; Zhang, C.; Lim, C. W.; Zhang, G. Z.; Yang, Z. B. A Gravity-Driven Sintering Method to Fabricate Geometrically Complex Compact Piezoceramics. *Nat. Commun.* **2021**, *12* (1), No. 6066.
(31) Chen, S. Y.; Li, J. P.; Shi, H. F.; Chen, X. L.; Liu, G.; Meng, S. H.; Lu, J. Lightweight and Geometrically Complex Ceramics Derived from 4D Printed Shape Memory Precursor with Reconfigurability and Programmability for Sensing and Actuation Applications. *Chem. Eng. J.* **2023**, *455*, No. 140655.
(32) Kong, D. K.; Guo, A. F.; Wu, H. L.; Li, X. J.; Wu, J. W.; Hu, Y. B.; Qu, P.; Wang, S. Q.; Guo, S. Four-Dimensional Printing of Polymer-Derived Ceramics with High-Resolution, Reconfigurability, and Shape Memory Effects. *Addit. Manuf.* **2024**, *83*, No. 104050.
(33) Zhang, D. W.; Peng, E.; Borayek, R.; Ding, J. Controllable Ceramic Green-Body Configuration for Complex Ceramic Architectures with Fine Features. *Adv. Funct. Mater.* **2019**, *29* (12), No. 1807082.
(34) Wang, Z. H.; Ma, D. H.; Wang, Y. H.; Xie, Y.; Yu, Z. H.; Cheng, J.; Li, L.; Sun, L.; Dong, S. X.; Wang, H. Kirigami-Origami-Inspired Lead-Free Piezoelectric Ceramics. *Adv. Sci.* **2023**, *10* (17), No. 2207059.
(35) Ahn, B. Y.; Shoji, D.; Hansen, C. J.; Hong, E.; Dunand, D. C.; Lewis, J. A. Printed Origami Structures. *Adv. Mater.* **2010**, *22* (20), 2251−2254.
(36) Ikushima, A. J.; Fujiwara, T.; Saito, K. Silica Glass: A Material for Photonics. *J. Appl. Phys.* **2000**, *88* (3), 1201−1213.
(37) Sugioka, K. *Microstructuring of Photosensitive Glass*; Springer Berlin, Heidelberg, 2012.
(38) Rahaman, M. N.; Day, D. E.; Bal, B. S.; Fu, Q.; Jung, S. B.; Bonewald, L. F.; Tomsia, A. P. Bioactive Glass in Tissue Engineering. *Acta Biomater.* **2011**, *7* (6), 2355−2373.
(39) Kotz, F.; Arnold, K.; Bauer, W.; Schild, D.; Keller, N.; Sachsenheimer, K.; Nargang, T. M.; Richter, C.; Helmer, D.; Rapp, B. E. Three-Dimensional Printing of Transparent Fused Silica Glass. *Nature* **2017**, *544* (7650), 337−339.
(40) Kotz, F.; Quick, A. S.; Risch, P.; Martin, T.; Hoose, T.; Thiel, M.; Helmer, D.; Rapp, B. E. Two-Photon Polymerization of Nanocomposites for the Fabrication of Transparent Fused Silica Glass Microstructures. *Adv. Mater.* **2021**, *33* (9), No. 2006341, DOI: 10.1002/adma.202006341.
(41) Bauer, J.; Crook, C.; Baldacchini, T. A. Sinterless, Low-Temperature Route to 3D Print Nanoscale Optical-Grade Glass. *Science* **2023**, *380* (6648), 960−966.
(42) Hong, Z. H.; Ye, P. A. R.; Loy, D. A.; Liang, R. G. Three-Dimensional Printing of Glass Micro-Optics. *Optica* **2021**, *8* (6), 904−910.
(43) Hong, Z. H.; Ye, P. R.; Loy, D. A.; Liang, R. G. High-Precision Printing of Complex Glass Imaging Optics with Precondensed Liquid Silica Resin. *Adv. Sci.* **2022**, *9* (18), No. 2105595.
(44) Wen, X. W.; Zhang, B. Y.; Wang, W. P.; Ye, F.; Yue, S.; Guo, H.; Gao, G. H.; Zhao, Y. S.; Fang, Q. Y.; Nguyen, C.; Zhang, X.; Bao, J. M.; Robinson, J. T.; Ajayan, P. M.; Lou, J. 3D-Printed Silica with Nanoscale Resolution. *Nat. Mater.* **2021**, *20* (11), 1506−1511.
(45) Huang, P. H.; Laakso, M.; Edinger, P.; Hartwig, O.; Duesberg, G. S.; Lai, L. L.; Mayer, J.; Nyman, J.; Errando-Herranz, C.; Stemme, G.; Gylfason, K. B.; Niklaus, F. Three-Dimensional Printing of Silica Glass with Sub-Micrometer Resolution. *Nat. Commun.* **2023**, *14* (1), No. 3305.
(46) Li, Z. Y.; Jia, Y. W.; Duan, K.; Xiao, R.; Qiao, J. Y.; Liang, S. Y.; Wang, S. X.; Chen, J. Z.; Wu, H.; Lu, Y.; Wen, X. W. One-Photon Three-Dimensional Printed Fused Silica Glass with Sub-Micron Features. *Nat. Commun.* **2024**, *15* (1), No. 2689.
(47) Li, M.; Yue, L.; Rajan, A. C.; Yu, L.; Sahu, H.; Montgomery, S. M.; Ramprasad, R.; Qi, H. J. Low-Temperature 3D Printing of Transparent Silica Glass Microstructures. *Sci. Adv.* **2023**, *9* (40), No. eadi2958.
(48) Hippler, M.; Blasco, E.; Qu, J. Y.; Tanaka, M.; Barner-Kowollik, C.; Wegener, M.; Bastmeyer, M. Controlling the Shape of 3D Microstructures by Temperature and Light. *Nat. Commun.* **2019**, *10*, No. 232.
(49) Hsu, L. Y.; Mainik, P.; Münchinger, A.; Lindenthal, S.; Spratte, T.; Welle, A.; Zaumseil, J.; Selhuber-Unkel, C.; Wegener, M.; Blasco, E. A Facile Approach for 4D Microprinting of Multi-Photoresponsive Actuators. *Adv. Mater. Technol.* **2023**, *8* (1), No. 2200801.
(50) Zeng, C.; Faaborg, M. W.; Sherif, A.; Falk, M. J.; Hajian, R.; Xiao, M.; Hartig, K.; Bar-Sinai, Y.; Brenner, M. P.; Manoharan, V. N. 3D-Printed Machines That Manipulate Microscopic Objects Using Capillary Forces. *Nature* **2022**, *611* (7934), 68−73.
(51) Py, C.; Reverdy, P.; Doppler, L.; Bico, J.; Roman, B.; Baroud, C. N. Capillary Origami: Spontaneous Wrapping of a Droplet with an Elastic Sheet. *Phys. Rev. Lett.* **2007**, *98* (15), No. 156103.
(52) Pokroy, B.; Kang, S. H.; Mahadevan, L.; Aizenberg, J. Self-Organization of a Mesoscale Bristle into Ordered, Hierarchical Helical Assemblies. *Science* **2009**, *323* (5911), 237−240.
(53) Kang, S. H.; Pokroy, B.; Mahadevan, L.; Aizenberg, J. Control of Shape and Size of Nanopillar Assembly by Adhesion-Mediated Elastocapillary Interaction. *ACS Nano* **2010**, *4* (11), 6323−6331.
(54) De Volder, M.; Hart, A. J. Engineering Hierarchical Nanostructures by Elastocapillary Self-Assembly. *Angew. Chem., Int. Ed.* **2013**, *52* (9), 2412−2425.
(55) Wang, Z. L.; Song, H. Y.; Xie, M. Z.; Zhan, Z. H.; Zhao, J. K.; Chen, Y. P. Programmable Self-Assembly of Microstructures on Mimicked Three Dimensional Functional Surfaces. *Mater. Today Phys.* **2023**, *38*, No. 101268.
(56) Lao, Z. X.; Hu, Y. L.; Zhang, C. C.; Yang, L.; Li, J. W.; Chu, J. R.; Wu, D. Capillary Force Driven Self-Assembly of Anisotropic Hierarchical Structures Prepared by Femtosecond Laser 3D Printing and Their Applications in Crystallizing Microparticles. *ACS Nano* **2015**, *9* (12), 12060−12069.
(57) Liu, X. J.; Wei, M. X.; Wang, Q.; Tian, Y. J.; Han, J. M.; Gu, H. C.; Ding, H. B.; Chen, Q.; Zhou, K.; Gu, Z. Z. Capillary-Force-Driven Self-Assembly of 4D-Printed Microstructures. *Adv. Mater.* **2021**, *33* (22), No. 2100332.
(58) Zhang, M. C.; Pal, A.; Lyu, X.; Wu, Y. D.; Sitti, M. Artificial-Goosebump-Driven Microactuation. *Nat. Mater.* **2024**, *23* (4), 560−569.
(59) Hu, Y. L.; Lao, Z. X.; Cumming, B. P.; Wu, D.; Li, J. W.; Liang, H. Y.; Chu, J. R.; Huang, W. H.; Gu, M. Laser Printing Hierarchical Structures with the Aid of Controlled Capillary-Driven Self-Assembly. *Proc. Natl. Acad. Sci. U. S. A.* **2015**, *112* (22), 6876−6881.
(60) Lao, Z. X.; Pan, D.; Yuan, H. W.; Ni, J. C.; Ji, S. Y.; Zhu, W. L.; Hu, Y. L.; Li, J. W.; Wu, D.; Chu, J. R. Mechanical-Tunable Capillary-Force-Driven Self-Assembled Hierarchical Structures on Soft Substrate. *ACS Nano* **2018**, *12* (10), 10142−10150.
(61) Hu, Y. L.; Feng, W. F.; Xue, C.; Lao, Z. X.; Ji, S. Y.; Cai, Z.; Zhu, W. L.; Li, J. W.; Wu, D.; Chu, J. R. Self-Assembled Micropillars Fabricated by Holographic Femtosecond Multi-Foci Beams for Trapping of Microparticles. *Opt. Lett.* **2020**, *45* (17), 4698−4701.
(62) Lao, Z. X.; Hu, Y. L.; Pan, D.; Wang, R. Y.; Zhang, C. C.; Ni, J. C.; Xu, B.; Li, J. W.; Wu, D.; Chu, J. R. Self-Sealed Bionic Long

Microchannels with Thin Walls and Designable Nanoholes Prepared by Line-Contact Capillary-Force Assembly. *Small* **2017**, *13* (23), No. 1603957.
(63) Hu, Y. L.; Yuan, H. W.; Liu, S. L.; Ni, J. C.; Lao, Z. X.; Xin, C.; Pan, D.; Zhang, Y. Y.; Zhu, W. L.; Li, J. W.; Wu, D.; Chu, J. R. Chiral Assemblies of Laser-Printed Micropillars Directed by Asymmetrical Capillary Force. *Adv. Mater.* **2020**, *32* (31), No. 2002356.
(64) Pan, D.; Liu, S. L.; Li, J. W.; Ni, J. C.; Xin, C.; Ji, S. Y.; Lao, Z. X.; Zhang, C. C.; Xu, B.; Li, R.; Fan, S. Y.; Li, P. J.; Hu, Y. L.; Wu, D.; Chu, J. R. Rapid Fabrication of 3D Chiral Microstructures by Single Exposure of Interfered Femtosecond Vortex Beams and Capillary-Force-Assisted Self-Assembly. *Adv. Funct. Mater.* **2022**, *32* (4), No. 2106917.
(65) Wu, D.; Ni, C. D.; Lao, Z. X.; Cao, Y.; Ni, J. C.; Ren, Z. G.; Liu, S. L.; Tao, Y.; Xin, C.; Pan, D.; Hu, Y. L.; Chu, J. R. Temperature-Regulated Bidirectional Capillary Force Self-Assembly of Femtosecond Laser Printed Micropillars for Switchable Chiral Microstructures. *ACS Nano* **2023**, *17* (13), 12820−12828.
(66) Wu, S. Z.; Li, X. K.; Liu, X.; Hu, H. J.; Dong, R.; Ni, J. C.; Pan, D.; Hu, Y. L.; Zhang, C. C.; Chen, C.; Zhang, Y. C.; Xia, H. J.; Wu, D.; Lao, Z. X. Light-Regulated Capillary Force Self-Assembly of Nano-Printed Pillars for Chiroptical Metamaterials. *Adv. Funct. Mater.* **2024**, *34* (44), No. 2407232.
(67) Lao, Z. X.; Liu, X.; Qi, Q. Q.; Hu, H. J.; Liu, M. Q.; Zhu, H. J.; Dong, R.; Zhang, Y. C.; Wu, S. Z.; Zhang, C. C.; Chen, C.; Zhang, L. Bidirectionally Symmetric Self-Assembly of Switchable Chiral Microstructures Based on Angle Compensation and Ph Regulation Strategy for Chiroptical Metamaterials. *Adv. Funct. Mater.* **2025**, *35*, No. 2423425.
(68) Wang, X. D.; Yu, H. B.; Yang, T.; Wang, X. F.; Yang, T.; Ge, Z. X.; Xie, Y. B.; Liao, X.; Li, P. W.; Liu, Z.; Liu, L. Q. Density Regulation and Localization of Cell Clusters by Self-Assembled Femtosecond-Laser-Fabricated Micropillar Arrays. *ACS Appl. Mater. Interfaces* **2021**, *13* (49), 58261−58269.
(69) Lao, Z. X.; Zheng, Y. Y.; Dai, Y. C.; Hu, Y. L.; Ni, J. C.; Ji, S. Y.; Cai, Z.; Smith, Z. J.; Li, J. W.; Zhang, L.; Wu, D.; Chu, J. R. Nanogap Plasmonic Structures Fabricated by Switchable Capillary-Force Driven Self-Assembly for Localized Sensing of Anticancer Medicines with Microfluidic Sers. *Adv. Funct. Mater.* **2020**, *30* (15), No. 1909467.
(70) Bauer, J.; Izard, A. G.; Zhang, Y. F.; Baldacchini, T.; Valdevit, L. Programmable Mechanical Properties of Two-Photon Polymerized Materials: From Nanowires to Bulk. *Adv. Mater. Technol.* **2019**, *4* (9), No. 1900146.
(71) Xu, Y.; Li, Y.; Zheng, N.; Zhao, Q.; Xie, T. Transparent Origami Glass. *Nat. Commun.* **2021**, *12* (1), No. 4261.
(72) Hong, Z. H.; Sun, Y. Y.; Ye, P. R.; Loy, D. A.; Liang, R. G. Bio-Inspired Compact, High-Resolution Snapshot Hyperspectral Imaging System with 3D Printed Glass Lightguide Array. *Adv. Opt. Mater.* **2023**, *11* (9), No. 2300156.
(73) Liu, Z. G.; Du, H. F.; Li, J. F.; Lu, L.; Li, Z. Y.; Fang, N. X. Nano-Kirigami with Giant Optical Chirality. *Sci. Adv.* **2018**, *4* (7), No. eaat4436.
(74) Gansel, J. K.; Thiel, M.; Rill, M. S.; Decker, M.; Bade, K.; Saile, V.; von Freymann, G.; Linden, S.; Wegener, M. Gold Helix Photonic Metamaterial as Broadband Circular Polarizer. *Science* **2009**, *325* (5947), 1513−1515.
(75) Hentschel, M.; Schäferling, M.; Duan, X. Y.; Giessen, H.; Liu, N. Chiral Plasmonics. *Sci. Adv.* **2017**, *3* (5), No. e1602735.
(76) Ni, J. C.; Liu, S. L.; Wu, D.; Lao, Z. X.; Wang, Z. Y.; Huang, K.; Ji, S. Y.; Li, J. W.; Huang, Z. X.; Xiong, Q. H.; Hu, Y. L.; Chu, J. R.; Qiu, C. W. Gigantic Vortical Differential Scattering as a Monochromatic Probe for Multiscale Chiral Structures. *Proc. Natl. Acad. Sci. U. S. A.* **2021**, *118* (2), No. e2020055118.
(77) Dai, N. W.; Liu, S. L.; Ren, Z. G.; Cao, Y.; Ni, J. C.; Wang, D. W.; Yang, L.; Hu, Y. L.; Li, J. W.; Chu, J. R.; Wu, D. Robust Helical Dichroism on Microadditively Manufactured Copper Helices Via Photonic Orbital Angular Momentum. *ACS Nano* **2023**, *17* (2), 1541−1549.
(78) Langenhorst, M.; Ritzer, D.; Kotz, F.; Risch, P.; Dottermusch, S.; Roslizar, A.; Schmager, R.; Richards, B. S.; Rapp, B. E.; Paetzold, U. W. Liquid Glass for Photovoltaics: Multifunctional Front Cover Glass for Solar Modules. *ACS Appl. Mater. Interfaces* **2019**, *11* (38), 35015−35022.
(79) Tatlisu, G. C.; Aciksari, C.; Celebi, S.; Turan, S. Developing a Hollow Glass Microsphere/Geopolymer Thermal Insulation Composite for Hot Metal Surface Coating. *Ceram. Int.* **2022**, *48* (9), 11924−11939.
(80) Miksa, B.; Trzeciak, K.; Kazmierski, S.; Rozanski, A.; Potrzebowski, M.; Rozga-Wijas, K.; Sobotta, L.; Ziabka, M.; Plódowska, M.; Szary, K. Nature-Inspired Synthesis of Yeast Capsule Replicas Encased with Silica-Vinyl Functionality: New Fluorescent Hollow Hybrid Microstructures. *Molecules* **2024**, *29* (22), No. 5363.
(81) Mansur, A.; Habibollahi, P.; Fang, A.; Mahvash, A.; Etezadi, V.; Liddell, R. P.; Camacho, J. C.; Cohen, E. I.; Kokabi, N.; Arepally, A.; Georgiades, C.; Nezami, N. New Frontiers in Radioembolization. *Ther. Adv. Med. Oncol.* **2024**, *16*, 1−22.
(82) Sigaev, V. N.; Atroschenko, G. N.; Savinkov, V. I.; Sarkisov, P. D.; Babajew, G.; Lingel, K.; Lorenzi, R.; Paleari, A. Structural Rearrangement at the Yttrium-Depleted Surface of Hcl-Processed Yttrium Aluminosilicate Glass for Y-Microsphere Brachytherapy. *Mater. Chem. Phys.* **2012**, *133* (1), 24−28.

https://doi.org/10.1021/acsnano.5c15343
ACS Nano 2025, 19, 40547−40560